2D LUNG THICKNESS ESTIMATION FROM CHEST X-RAYS USING U-NET REGRESSION TRAINED WITH DIGITALLY RECONSTRUCTED RADIOGRAPHS

Thesis

Submitted to

The School of Engineering of the

UNIVERSITY OF DAYTON

In Partial Fulfillment of the Requirements for

The Degree of

Master of Science in Computer Engineering

By

John Joseph Marsh III

Dayton, Ohio

May, 2024

2D LUNG THICKNESS ESTIMATION FROM CHEST X-RAYS USING U-NET REGRESSION TRAINED WITH DIGITALLY RECONSTRUCTED RADIOGRAPHS

Name: Marsh III, John Joseph

APPROVED BY:

Russell C. Hardie, Ph.D.
Advisory Committee Chairman
Professor and Chair, Electrical and Computer Engineering

Amy Neidhard-Doll, Ph.D.
Committee Member
Associate Professor, Electrical and Computer Engineering

Barath Narayanan, Ph.D.
Committee Member
Adjunct Professor and Research Scientist, Electrical and Computer Engineering and University of Dayton Research Institute

ABSTRACT

2D LUNG THICKNESS ESTIMATION FROM CHEST X-RAYS USING U-NET REGRESSION TRAINED WITH DIGITALLY RECONSTRUCTED RADIOGRAPHS

Name: Marsh III, John Joseph
University of Dayton

Advisor: Dr. Russell C. Hardie

Chest X-rays (CXRs) are one of the most common medical imaging procedures providing two-dimensional (2D) images of three-dimensional (3D) density data regarding a patient's chest. Computed tomography (CT) scans give a more extensive look at a desired location by utilizing X-rays to provide a 3D view of a specified area of the human body in slices. CT scans are quintessential for getting lung measurements as well as identifying and tracking lung cancer nodule growth within said lungs. Many different computer aided detection (CAD) systems have the ability to read CT scan data and assist medical professionals in outlining essential information within the lungs such as providing lung outlines, detecting lung nodules, and more. The ability for a CAD system to take advantage of lung thickness information would assist with bounding CAD systems but also providing algorithms with information that can assist in determining the likelihood of a nodule present in certain lung areas. In this approach, a method by which CT scans are converted into synthetic CXRs is introduced. In the process of generating these synthetic CXRs, a corresponding set of relative 2D lung thickness values is generated for each pixel in which the lung exists within a scan as a beam travels through the lung from front to back. A regression neural network (RNN) is then created based on U-Net architecture to train a model to predict the relative thickness of the lungs using the data from the synthetic CXR generation. CT scans from

the Lung Image Database Consortium-Image Database Research Initiative (LIDC-IDRI) are used to generate synthetic CXRs and the associated lung thickness data. After the data has been processed, scaled, and augmented, it is used to train and test the U-Net RNN, which can predict relative lung thickness in other synthetic CXRs with an overall mean absolute error (MAE) of 0.0301 and an overall mean squared error (MSE) of 0.0047.

To my friends, who always support me when the going gets tough. To my family, who always present encouragement and advice. And most importantly, to my loving wife, Haley, who inspires and motivates me in everything I do.

ACKNOWLEDGMENTS

I would like to acknowledge and thank my professors, Dr. Russel Hardie, my Thesis Advisor, and Dr. Barath Narayanan, a research engineer at UDRI. Both were instrumental in my growing passion and understanding of machine learning, neural networks, deep learning, and many other AI concepts as well as image and signal processing. Secondly, I would like to thank the University of Dayton (UD) for supporting me in my undergraduate and graduate degrees. Their academic curriculum always strived to challenge my understanding of the world around me and helped me to grow myself as well. Furthermore, I would also like to acknowledge the Department of Defence's (DoD's) SMART Scholarship Program for providing support for both my undergraduate and graduate degrees, both in terms of their financial assistance as well as their providing of numerous mentors at the Air Force Research Labs who have assisted in my growth as an Electrical and Computer Engineer. Finally, for all those who have also assisted me in this process of academia that I did not already mention. Every portion of support, no matter how large or small, has taken me to where I am today. Because of that, I thank you.

TABLE OF CONTENTS

LIST OF FIGURES

LIST OF TABLES

LIST OF VARIABLES

- β - Boosting of X-ray Absorption through Simulated Tissue Density
- I - Beam Intensity
- I_0 - Incident Beam
- x - Beam's Travelled Distance
- A - Attenuation Coefficient
- $\mu_{av}(x, z)$ - Attenuation Coefficient through x and z Planes
- μ_{water} - Attenuation Coefficient for Water
- μ_{air} - Attenuation Coefficient for Air
- $CT(x, y, z)$ - CT Data in Three Dimensions
- $I_{out}(x, z)$ - Output Beam Intensity Travelling through x and z Planes
- I_{in} - Incoming Incident Beam

LIST OF ACRONYMS

- 3D - 3-Dimensional
- ACGAN - Auxiliary Classifier Generative Adversarial Network
- AI - Artificial Intelligence
- CAD - Computer-Aided Detection
- CNN - Convolutional Neural Network
- CR - Chest Radiograph
- CT - Computed Tomography
- CXR - Chest X-ray
- DICOM - Digital Imaging and Communications in Medicine
- DRR - Digitally Reconstructed Radiograph
- FCNN - Fully Convolutional Neural Network
- GAN - Generative Adversarial Network
- HU - Hounsfield Unit
- LIDC-IDRI - Lung Image Database Consortium Image Database Research Initiative
- MAE - Mean Absolute Error
- mm - millimeters
- MSE - Mean Squared Error

- NBIA - National Biomedical Imaging Archive
- PFT - Pulmonary Function Test
- PGGAN - Progressively Growing Generative Adversarial Network
- PSNR - Peak Signal-to-Noise Ratio
- PUNet - U-Net for Pansharpening
- RMSE - Root Mean Squared Error
- RNN - Regression Neural Network
- SSIM - Structural Similarity

CHAPTER I

INTRODUCTION

Chest X-Rays (CXRs) are a common medical imaging procedure that provides two-dimensional (2D) images of three-dimensional (3D) density data of the chest. These images are used to detect and evaluate numerous lung conditions such as pneumonia, COVID-19, tuberculosis, lung cancer, and lung tissue scaring [1], [2]. However, for more invasive issues, more complex, detailed techniques are required, which is where computed tomography (CT) scans are best equipped. CT scans take X-rays and deploy them into scanning slices of an area which are then compiled into a 3D rendition of the area scanned. While a great source of information, CT scans prove to be more expensive and expose the patient to a much higher dose of radiation compared to that of a CXR. Because of this, methods to extract as much information from CXR images is an increasing desire within the medical imaging community. This can range from detecting lung nodule growth or infections as well as lung volume estimation [3].

Automated lung segmentation is a task in CXR analysis that comes with great importance as it is a prerequisite step for many analysis methods [4]. The lung boundary that is created in the process of lung segmentation may be employed to limit the search for lung ailments using different algorithms for lung image analysis, specifically to ensure that false alarms coming from outside the lung are inhibited [5]. To our knowledge, only one prior work has investigated the estimation of lung thickness information using machine learning algorithms from CXR data. Lung thickness information would be useful for not only bounding computer aided detection (CAD) algorithms, but also providing them with valuable information about the amount of lung present at each 2D position of the lung itself. This could be especially useful in the detection of lung nodules where low lung thickness

could indicate a lower likelihood of lung nodule presence and vice versa. This could be highly salient information for CAD systems in their process of searching for lung disease as well. Furthermore, the lung thickness data gives more information for the system and its users to analyze regarding lung morphology as well as lung volume. The most efficient means to create this lung thickness data as well as train the network is to use CT scans to create synthetic CXRs, not to be confused with artificially generated CXRs.

Artificially generated CXRs are fundamentally different than synthetic CXRs. Artificial CXR generation is the idea of generating completely artificial data using a few examples of real CXRs. One such method to accomplish this is the use of Generative Adversarial Networks (GANs) which, by extrapolating key features from example data, can generate completely synthetic outputs. Segal et al. [6] evaluated the difference in clinical realism between artificially generated CXRs and real CXRs utilizing a Progressive Growing GAN (PGGAN). Karbhari et al. [7] developed an Auxiliary Classifier Generative Adversarial Network (ACGAN) in an attempt to create CXRs both with positive and negative diagnoses of COVID-19. Positive and negative COVID-19 cases were inputted into an ACGAN with the artificial outputs being utilized as additional training data for a COVID-19 classifier. By introducing the artificial CXR data into the training pool, the classification results improved across the board.

Synthetic CXRs, or digitally reconstructed radiographs (DRRs), are created using real data as their basis. The fundamental idea is that the sliced layers of a CT scan can be mathematically converted to appear as if a singular X-ray beam passed through each layer. This essentially flattens the CT data and outputs a synthetic CXR. The generation of DRRs from CT data has been around since before the turn of the century as seen in Galvin et al. [8], who desired to use the DRRs to assist in three-dimensional (3D) treatment planning.

Methods in which these DRRs are generated have changed over the years with different methods discussed.

DRR generation is a very open-ended subject as the results depend solely on how researchers choose to go about the creation of the data itself. Different researchers will approach the task in different ways. Li et al. [9] utilizes six different parameters consisting of three variables expressing translations and three expressing rotations, which were then used with the 3D Bresneham line generation algorithm. Staub et al. [10] utilize a method in which the CT numbers were converted to linear attenuation coefficients with scatter, beam hardening, and veiling glare removed from the attenuations before the conversion and re-added in post-processing. In [11], [12], and [13], a parallel projection model with linear attenuation coefficients included was utilized to simulate the X-rays from the CT data. DRRs are becoming so inundated in the medical imaging space that people are focused on optimization as well as further integration into existing systems. Dorgham et al. [14] gives a detailed explanation in which a 50% accelerated rendering of DRRs is achieved with the help of a proposed automatic body segmentation method. Lance Levine and Mark Levine [15] published an extension for a popular CT imaging reader, called 3D Slicer, which allows for a free, open-source means by which one can generate DRRs from CT data directly from the application. With the rise in popularity of DRR generation, these methods in synthetic CXR creation are being applied to train different neural networks within the medical field.

The idea of integrating generated DRRs with AI techniques is becoming more and more prominent within the medical imaging community. In [11], the emphysema percentage of a patient was analyzed with the use of simulated CXRs as well as a convolutional neural network (CNN). In [12], lung structures were enhanced within DRRs with the help of a fully convolutional neural network (FCNN) to create more accurate synthetic images. Both give

an in-depth look at the process of the mathematical portion of DRR generation but also use the DRRs with machine learning algorithms to extrapolate additional information that would otherwise go unlooked. Each uses its respective type of neural network architecture to accomplish the aforementioned research with one using a CNN and another choosing an FCNN. Sogancioglu et al. [16] utilize different transfer learning architectures and networks with the purpose of regression on synthetic CXRs to predict the total lung volume from CXRs rather than calculating it from the pulmonary function test (PFT).

As touched upon, varied network architectures and structures can be used to achieve different objectives. U-Nets, a CNN architecture, are popular for semantic segmentation and classification because of their data efficiency and performance, which is explained in more detail in [17]. This architecture continues to be built upon almost a decade later. In [18], a computationally efficient means by which chest radiographs (CRs) are semantically segmented via the use of U-Net-based networks is detailed. In this way, a CR is outlined by the network to find the boundaries of the total set of lungs, which potentially can assist medical professionals in structural analysis of the lungs as well as diagnosis. In other implementations, U-Nets are trained to segment other growths or changes as well as the lungs themselves using CXRs and CT scans. In [19], a 3D U-Net is trained along with other network implementations to segment 3D sections of CT scans as well as potential COVID-19 infection areas within the lungs themselves. In this way, the network is trained to intake CT scans and give a narrowed view of areas of interest for the doctors. Past this, U-Nets are also popular in their adaptation toward other uses as well.

The U-Net architecture is adapted for other uses past just segmenting or classifying. In [13], bone structures were extracted from DRR images to train a U-Net to create enhancements, specifically the creation of skeletal structures, for less detailed DRRs. U-Nets

can also be fundamentally modified to output different kinds of results. Image-to-image regression is performed by taking a U-Net and replacing its final layers with one that utilizes some form of mean squared error (MSE) to give pixel-level estimations. The benefits of a U-Net are still present with its computational efficiency and performance. However, rather than attempting to classify an image or performing semantic segmentation to classify different sets of pixels, the U-Net predicts a continuous value at each pixel in the output. In [20], a pixel-wise regression utilizing a U-Net architecture is deployed to create U-Net for Pansharpening (PUNet), which gives excellent performance compared to other provided pansharpening networks. In [21], two multitask networks, which use U-Net and HRNet respectively, to segment the lungs created via a DRR conversion process from the posteroanterior view and the lateral view to then estimate lung volume capacity. Of interest was the use of volume ratios to train the regression aspects of the two networks, which allowed for much greater accuracy predictions.

Similarly, CT data is usable in creating DRRs as well as generating 2D lung thickness data. With that, a network can be trained to utilize a synthetic CXR to predict the 2D lung thickness, which can then be viewed in 3D space. This can assist in viewing different abnormalities on the lungs' outer surface as well as determining the approximate lung thickness. This technology could assist in procedures like lung transplants, as donor lung size is an essential factor when determining donor-recipient compatibility. In many ways, the concept could act as a compression factor for physicians and medical professionals to glean more information from less physical data, saving time and money. However, a primary motivator is the ability to integrate predicted relative lung thickness values from a CXR into CAD algorithms, specifically as it relates to detecting lung nodules as well as assisting in areas of lung morphology. By integrating relativized lung thickness values, CAD algorithms

could further remove potential false positives by using the thickness of the lung at any given position to increase or decrease the likelihood of nodule growth, with thicker areas indicating higher percentages of nodule growth and thinner areas indicating lower percentages.

CAD systems with their associated tools and algorithms are a point of research that has attracted many within the past several years in an attempt to perfect methods of information extraction via CT scans and CXRs {[18], [22], [23], [24], [25], [26], [27], [28], [29], [30], [31], [32], [33], [34], [35], [36], [37], [38], [39], [40], [41], [42], [43], [44], [45], [46], [47], [48], [49], [50]}. Different methods by which these systems and their tools can be improved is a topic of intense study, especially with integrations of different deep learning techniques. By utilizing a 3D lung segmentation algorithm, as well as some other internal tools via the CAD, FlyerScan, which was developed by the University of Dayton Research Institute, relative 2D lung thickness values are derived from the data found in CT scans. These values can then be utilized with DRRs derived from CT scans to train a U-Net designed for regressions that predicts the relative 2D lung thickness values directly from a CXR. In [51], pixel-wise thickness maps are created along with synthetic CXRs from CT scans in the Luna16 dataset, a subset of the LIDC-IDRI database, to predict total lung volume utilizing two different U-Nets, one of which predicted the segmented the lungs to generate lung masks that could indicate area and the other U-Net with a linear activation function that enabled an image-based regression. The outputs of the two in conjunction with a corrective factor and a patient-specific posterior-anterior diameter measurement from the original set of lungs allowed for relatively accurate total lung volume predictions.

Rather than employing two separate U-Nets to derive total lung volume, a singular convolutional neural network is designed using a base U-Net architecture. However, a modification to the standard design replaces its softmax layer and its final output layer with

a singular regression layer. As will be seen in the following sections, the U-Net regression network for this project is designed to be larger and more complex, comprising a total of 5 layers with its final output regression layer utilizing half mean squared error. Focusing on the accuracy of the relative 2D lung thickness maps allows for an extremely accurate relative prediction of lung thickness across the space of the 2D lung boundaries. This information has the potential to provide CAD tools, such as lung nodule detectors or lung morphology generation algorithms, with in-depth 3D predictions from a singular 2D image. The data could provide quintessential contextual information that lung nodule detection algorithms in particular could integrate that allow for relative lung thickness predictions to increase the likelihood of nodule growth in thicker lung regions or to decrease the prediction odds of a nodule if in a thinner region or the edge of the lung.

CHAPTER II

MATERIALS

In this thesis, the data that is utilized to convert CT scans to DRRs as well as generate relative lung thickness values is from the Lung Image Database Consortium-Image Database Research Initiative (LIDC-IDRI) database which was provided at the National Biomedical Imaging Archive (NBIA) [38]. Created by the National Cancer Institute, the database was enhanced by the Foundation of the National Institutes of Health as well as the Food and Drug Administration [38]. This database is publicly available with the purpose of developing Computer-Aided Detection (CAD) systems that utilize CT scans as its primary motivation, especially in the area of lung nodule detection [38]. The LIDC-IDRI database is a reliable and stable resource for medical imaging researchers, and in recent years, it has become a primary resource for the training and testing of different AI models with a wide variation of architectures and processing techniques to test new ideas and concepts.

Within the LIDC-IDRI dataset, there are 1018 CT scans from 1010 unique patients that are each segmented by a team of radiologists included in the project [38]. The radiologists segment not just the lungs of the patients but also the nodules that were detected in each of the CT scans. With a total of 1018 scans, each has the lungs and the respective nodules of each lung segmented with the generalized truth of each segmentation coming out to be where the majority of the radiologists agreed at each pixel overlap. Of these 1018 scans, 1017 of them are utilized in the process of CT to DRR conversion with the accompanying relative 2D lung thickness values also calculated. This is done via the Digital Imaging and Communications in Medicine (DICOM) data providing the categorized information such as CT slices and sizing variables. In one of the CT scans within the LIDC-IDRI, a slice thickness value was set to zero within the scan's metadata. Consequently, it is omitted from

the number of overall CT scans available to convert, leaving the total number of 1017 scans used.

CHAPTER III

METHODOLOGIES

3.1 Synthetic CXR and Lung Thickness Generation

The process of converting a CT scan to a DRR relies on a method based on the work of Ophir Gozes and Hayit Greenspan [13] as well as an understanding of the DICOM formatting process for CT scans and of the Hounsfield scale. A quintessential concept regarding X-rays is that as they travel through matter, the energy continues to decrease with said decrease relying on the distance that the X-ray travels as well as the attenuation coefficient. The specifics of this interrelation are shown in Beer Lambert's law:

$$I = I_0 \exp^{Ax} \tag{1}$$

where I is the intensity of the beam with I_o as the incident beam, x being the distance traveled by the beam, and A being the attenuation coefficient [13]. A diagram of how this applies in physical space is seen in Figure 3.1. Using the same variables as above, Beer Lambert's law is visualized with both a single attenuation material and distance as well as multiple, thereby detailing how an X-ray beam moves from its point of origin across one or multiple attenuation coefficients at the respective distances of each, it ends up as slightly decayed in its magnitude when it reaches it detection point. It is for this reason that X-rays show 3D density data for patients in a 2D image as the beam reflects differently based on the material it passes through whether that is air-filled lung or calcium-rich bone.

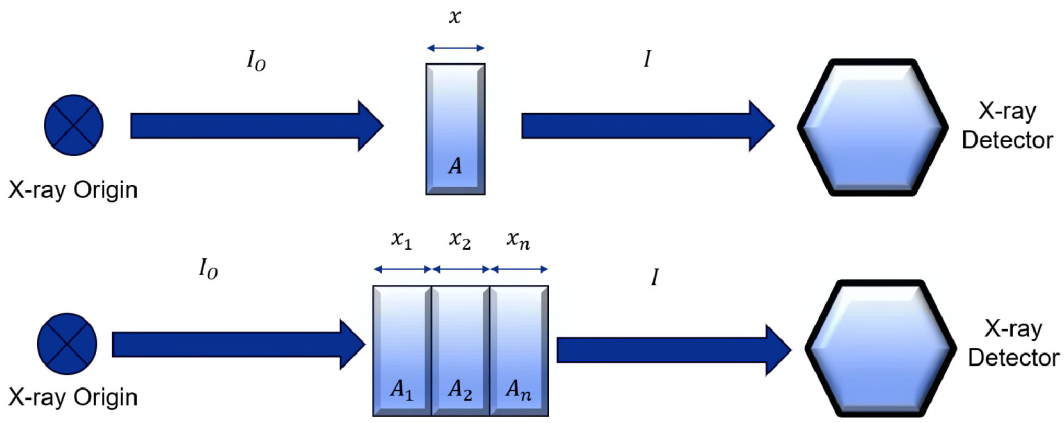

Figure 3.1: Diagram detailing the practical working of Beer Lambert's law with variations for single or multiple materials that an X-ray beam passes through moving from its origin to the X-ray detector. Each of the materials that a beam passes through has its respective attenuation coefficient and distance that the beam travels, which is denoted with subscript numbers on x and A. The top portion of the diagram shows a single attenuation material while the bottom shows multiple.

For a CT scan to be artificially converted into a CXR, each voxel of the CT scan undergoes a calculation for their respective attenuation coefficients. Each present voxel is given by its Hounsfield Unit (HU) which represents the original linear attenuation coefficient following a linear transformation [13]. Because of this, the values that constitute the linear attenuation are preserved. A parallel project model is utilized with a computation for the average attenuation coefficient occurring in line with the y-axis with a range of [1,N] with the N denoting pixel length of the posterior-anterior view [13]. Utilizing the attenuation coefficient of water, μ_{water}, the attenuation coefficient of air, μ_{air}, and the CT volume, $CT(x, y, z)$, the following equation is utilized to compute the 2D average attenuation map:

$$\mu_{av}(x, z) = \sum_{y=1}^{N} \frac{(\mu_{water} - \mu_{air})(CT(x, y, z) + \mu_(water))}{(N \cdot 1000)}. \tag{2}$$

From that, Beer Lambert's law from Equation 1 and Equation 2 are combined to get Equation 3:

$$I_{out}(x,z) = I_{in} \exp^{\beta \cdot \mu_{av}(x,z)} . \tag{3}$$

Utilizing Equations 1 through 3, the only missing components round out to be β, μ_{water}, and μ_{air}. The linear attenuation for water and air are 0.2 cm^{-1} and 0 cm^{-1} respectively. β, which designates the boosting of X-ray absorption through simulated tissue density, is set to 1 [52]. Of note, the β allows for differing views of the synthetic CXR specifically in which aspects of the CT data come through the most in the DRR outputs. While 1 is used, differing values potentially focus on different aspects of the scan, with different values focusing on aspects of the average 2D attenuation map for the scan; different values would clarify certain aspects of the body compared to others such as having an option to see more bone structure than lung area.

With the ability to generate DRRs examined, the next step becomes to properly create the DRR and the lung thickness arrays. The DRRs are generated using the data from the LIDC-IDRI DICOM CT scans which are inserted into Equation 2 to get the average 2D attenuation map for each of the CT scans. These maps are then used with Equation 3, which is the derived Beer Lambert's law, to properly output a DRR image. Once the synthetic CXRs are generated, the lung thicknesses are created by taking the CT data and first applying a 3D lung segmentation algorithm to it. The output 3D lung segmentation matrix is then put through the same Beer Lambert's law derivation by getting the average 2D attenuation map via Equation 2 for the 3D lung segmentation followed by merging it

into Equation 3. Visualizations showing the creation of the synthetic CXRs and the 2D lung thickness value arrays are seen in Figures 3.3 and 3.2.

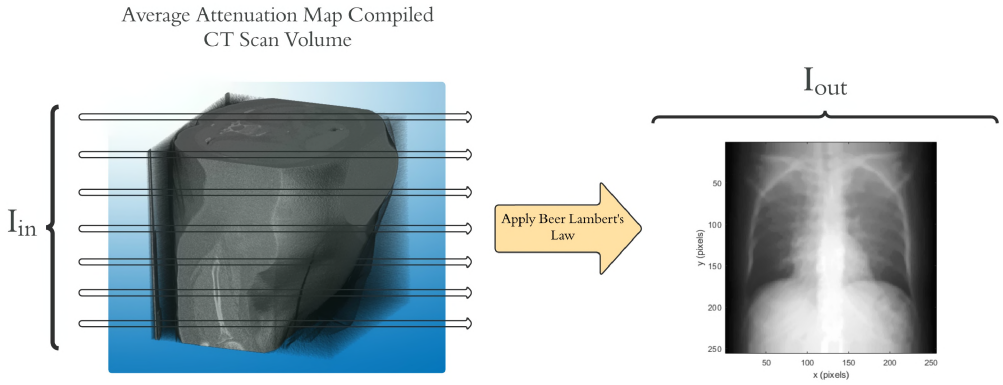

Figure 3.2: Visualization of the average attenuation map across the CT scan volume followed by processing it with the derived Beer Lambert's law to get the normalized synthetic CXRs (DRRs).

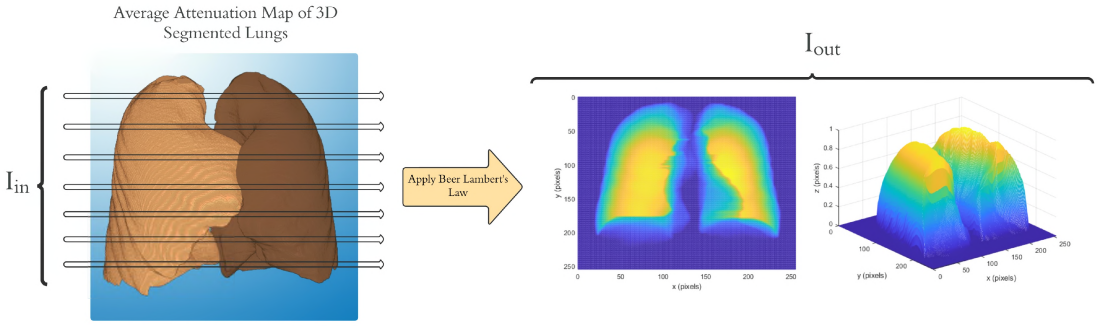

Figure 3.3: Visualization of the average attenuation map across the 3D segmented lung volume created with CAD algorithms followed by processing with the derived Beer Lambert's law to get the relative 2D lung thickness arrays.

Figures 3.2 and 3.3 give a visualization of the synthesized X-ray beams across the average attenuation maps calculated from the compiled CT scan volumes and the 3D segmented lung volumes followed by the application of Beer Lambert's law to get normalized synthetic CXRs and relative 2D lung thickness arrays. As a final step before the saving of the lung thickness and DRRs, the synthetic CXR is normalized by its highest values with the lung thickness values converted from millimeters to relative values ranging from [0,1]. These two measures allow for less variation for the network to train against with much better performance occurring after these measures are taken. The normalized synthetic CXR and the relative lung thickness array are then resized to $256x256$, which is the desired input size of the U-Net with a later explanation given in Section 3.2. A flowchart detailing the move of CT information starting at the LIDC-IDRI DICOM data to the creation of synthetic CXRs and relative lung thickness values is seen in Figure 3.4.

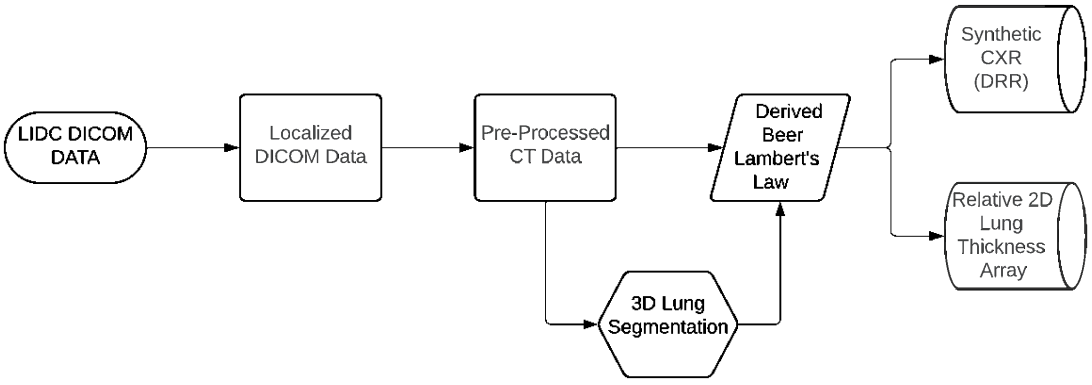

Figure 3.4: Flowchart detailing the moving from LIDC-IDRI DICOM data, which contains the CT slice information of 1018 patients, to the creation of synthetic CXRs (DRRs) and relative 2D lung thickness values

As seen in Figure 3.4, the desired CT data starts in the LIDC-IDRI DICOM format, which is downloaded and pre-processed into the CT data that is desired. From there, the CT data is placed into the derived Beer Lambert's law via Equations 2 and 3. This gives an output of the desired DRRs. In order to get the relative 2D lung thickness arrays, the CT data is first placed into the 3D lung segmentation algorithm and then placed into the derived Beer Lambert's law, which gives the lung thickness arrays. An example of a synthetic CXR following a histogram equalization and a relative lung thickness array can be seen in Figures 3.5 and 3.6.

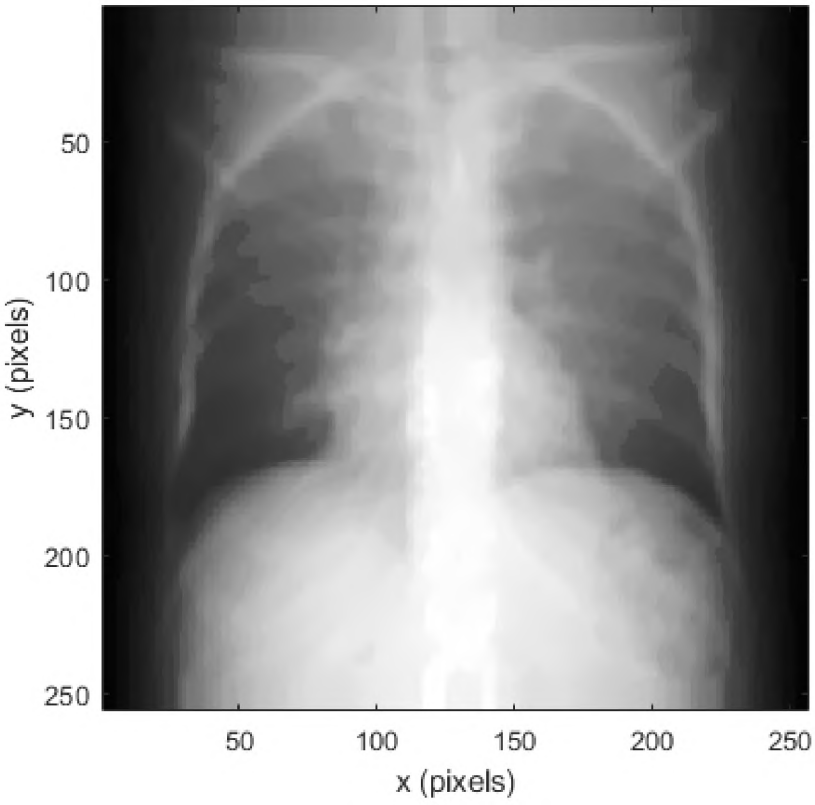

Figure 3.5: Synthetic CXR, or DRR, example sized at $256x256$ for the training and testing of the U-Net RNN. This example is LIDC-IDRI case 0531 for reference. This image is shown following a histogram equalization for better visualization.

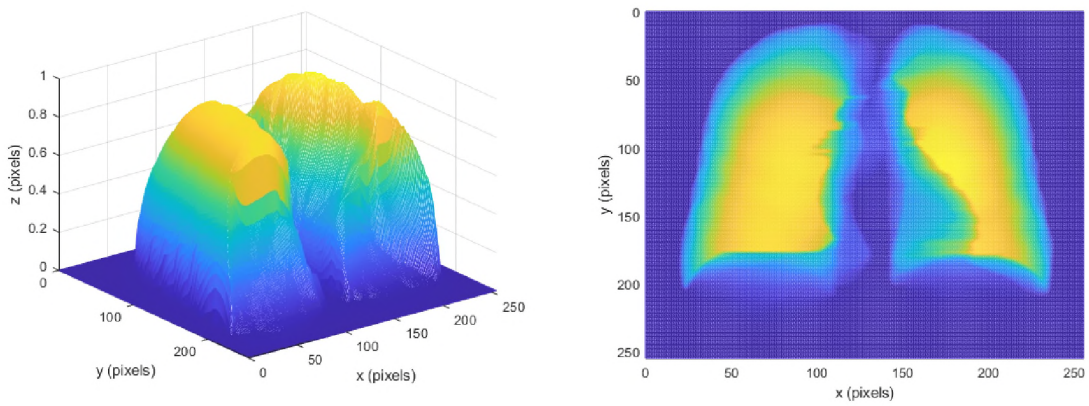

(a) (b)

Figure 3.6: This shows the relative, 2D lung thickness input array in 3D space with the following views: (a) Sagittal-Coronal plane view and (b) Coronal/Frontal plane view. The case used is LIDC-IDRI case 0531.

Figure 3.5 shows a synthetic CXR generated from the LIDC-IDRI CT data, which is to be used as an input image into the network that is to be trained. The image seen above is post-histogram equalization to better visualize the lungs following the CT to synthetic CXR conversion. Figure 3.6 shows the relative 2D lung thickness in 3D space from the sagittal-coronal plane of the lungs on the left and the coronal plane view on the right. The lung thickness, originally calculated in millimeters, is scaled from [0,1] to increase compatibility.

3.2 U-Net Regression Network

U-Net is a CNN architecture that has different encoder and decoder units paired in a U-shape acting as convolutional layers. In the first half of the U, encoder layers downsample the input image/array to get a smaller and smaller feature map that is ported to the corresponding decoder layer on the opposite side of the U; on the right side, or the decoder side, of the U, the feature maps generated during the encoding process are utilized to

decode said maps by upsampling the encoder layers' outputs [17]. Because of the U-Net design, many different leaps in semantic segmentation performance in neural networks are achieved with a lesser number of training images able to produce more precise results than were previously possible. U-Net also is able to withstand more variations in data, making deformations or abnormalities in different medical images less impactful than in previous designs. The design for the proposed U-Net RNN is seen in Figure 3.7.

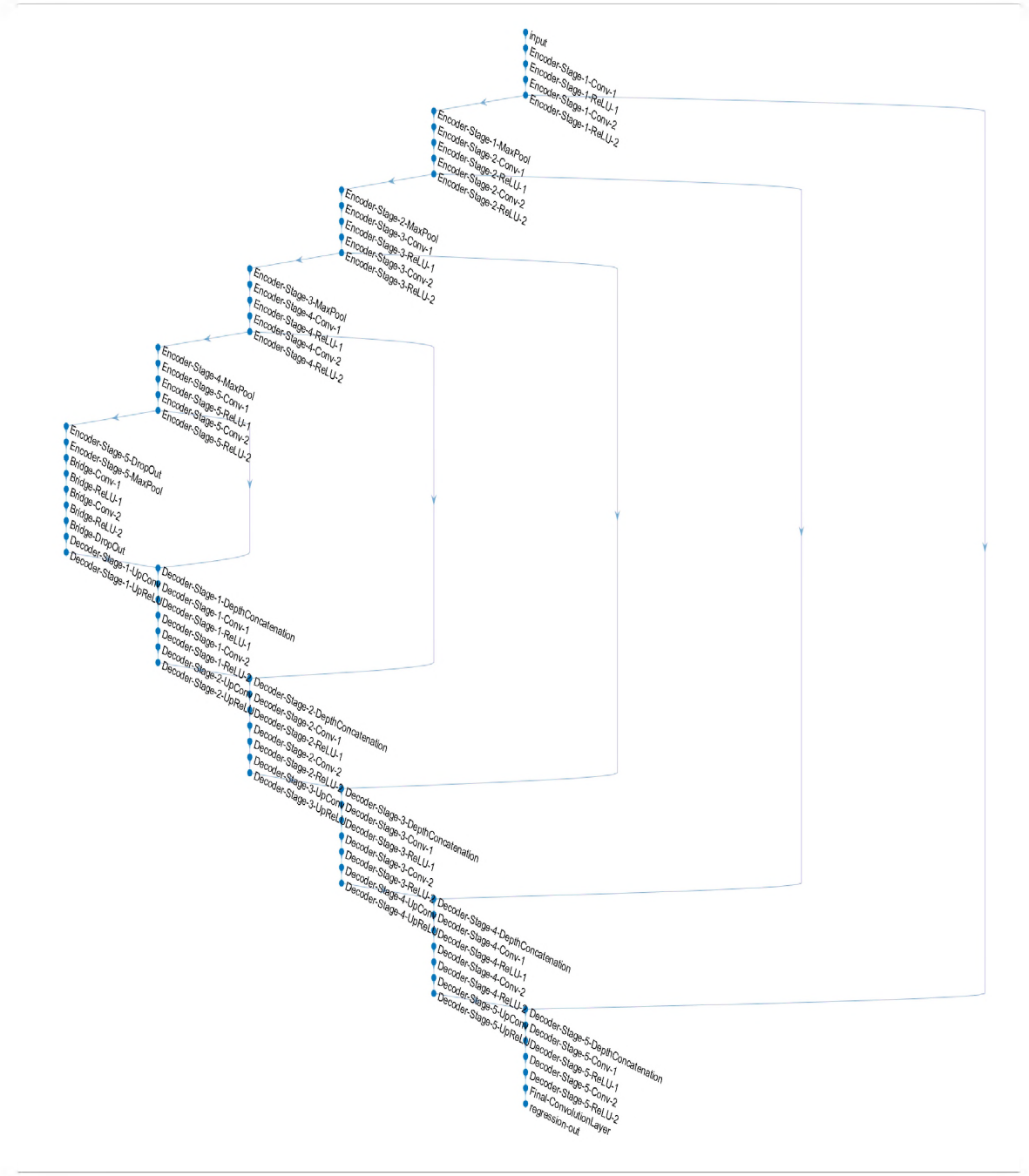

Figure 3.7: Shown is the structure of the U-Net Regression Neural Network, which includes 5 layers as well as a regression output. This structure is a rather simple design following a typical U-Net with a $256x256x1$ input and ending with a $256x256x1$ regression output with predicted regression values reflecting the model's predictions of the relative lung thickness data.

Figure 3.7 shows the U-Net architecture in the proposed RNN. Of particular difference between a standard U-Net used for classification is the removal of the final softmax layer as well as a classification layer in exchange for a regression layer that employs half mean squared error loss. This allows for the benefits of the U-Net architecture with its flexibility in data learnability while allowing for the network to give variable values along the predicted output array. The images used are $256X256$ in size with 64 filters in the first convolution layer, with the network coming out to be five layers real. All convolution operations that are performed in the network are $3x3$ with the max pooling set to be $2x2$ with a stride of 2. Up-convolutions and bridge convolutions are performed with the deconvolution layers performing deconvolutions as well as unpooling operations that ensure the upscaling of the feature map for U-Net learning. For this design, the initial learning rate is set to 0.001 utilizing the 'Adam' optimization algorithm and having the max epochs set at 25. Tables 3.1 through 3.4 show the parameter list in every one of the convolution layers included in the 5-layer U-Net, which includes the encoding, decoding, bridge, and up-convolutions stages of the layers.

Table 3.1: Parameters during Encoding for Convolutional Layers in 5-Layer U-Net RNN

Encoding Stages		Number of Filters	Parameters (Excluding Bias)
Stage	Conv. #		
1	1	64	3 x 3 x 1 x 64
1	2	64	3 x 3 x 64 x 64
2	1	128	3 x 3 x 64 x 128
2	2	128	3 x 3 x 128 x 128
3	1	256	3 x 3 x 128 x 256
3	2	256	3 x 3 x 256 x 256
4	1	512	3 x 3 x 256 x 512
4	2	512	3 x 3 x 512 x 512
5	1	1024	3 x 3 x 512 x 1024
5	2	1024	3 x 3 x 1024 x 1024

Table 3.2: Parameters during Decoding for Convolutional Layers in 5-Layer U-Net RNN

Decoding Stages		Number of Filters	Parameters (Excluding Bias)
Stage	Conv. #		
1	1	1024	3 x 3 x 2048 x 1024
1	2	1024	3 x 3 x 1024 x 1024
2	1	512	3 x 3 x 1024 x 512
2	2	512	3 x 3 x 512 x 512
3	1	256	3 x 3 x 512 x 256
3	2	256	3 x 3 x 256 x 256
4	1	128	3 x 3 x 256 x 128
4	2	128	3 x 3 x 128 x 128
5	1	64	3 x 3 x 128 x 64
5	2	64	3 x 3 x 64 x 64

Table 3.3: Parameters for Bridge Convolution Layers in 5-Layer U-Net RNN

Bridge Convolution #	Number of Filters	Parameters (Excluding Bias)
1	1024	3 x 3 x 1024 x 2048
2	2048	3 x 3 x 2048 x 2048

Table 3.4: Parameters for Up-Convolution Layers in 5-Layer U-Net RNN

Decoding Stage #	Number of Filters	Parameters (Excluding Bias)
1	1024	2 x 2 x 1024 x 2048
2	512	2 x 2 x 512 x 1024
3	256	2 x 2 x 256 x 512
4	128	2 x 2 x 128 x 256
5	64	2 x 2 x 64 x 128

3.2.1 Data Augmentation

To create more training data with additional variation, augmentation techniques are applied to the LIDC-IDRI data. While only slight, the augmentation allows for the increased accuracy of the training thanks to an increased pool of data which the U-Net RNN can use to train. To provide realistic changes that would not skew the data too far from the original data pool, only small augmentations are applied. The data is given the following augmentations: scaling from [0.9, 1.1], x-translation from [-2.5, 2.5], and y-translation from [-2.5, 2.5].

CHAPTER IV

EXPERIMENTAL RESULTS AND DISCUSSION

In total, 1017 CT scans of the 1018 that appear in the LIDC-IDRI database are used, which are split between training, validation, and testing data categories. Each of the 1017 CT scans is utilized to generate one DRR and one relative 2D lung thickness array respectively. The separation of the LIDC-IDRI CT scan data into the different network splits is seen in Table 4.1.

Table 4.1: LIDC-IDRI CT Scans Split between Training, Validation, and Testing Cases

Network Version	**LIDC-IDRI CT Scans**		
	Training Cases	**Validation Cases**	**Testing Cases**
U-Net RNN (95/5 Split)	864	102	51
U-Net RNN (90/10 Split)	864	51	102
U-Net RNN (80/20 Split)	783	31	203

Table 4.1 shows how each of the LIDC-IDRI CT scans is split for each of the trained networks for the training, validation, and testing pools. For the 95/5 split network, the training data utilizes 864 cases, the validation uses 102 cases, and the remaining 51 cases are used for testing while in the 90/10 split network, the training cases remain the same with the testing cases and validation cases swapping values. Finally, the 80/20 split network uses 783 scans for training, 31 for validation, and 203 for testing. The smaller validation number was done to keep with the minimum amount of validation cases needed to match the number of training cases in network training.

The results of the U-Net RNN networks are measured with MSE, mean absolute error (MAE), root mean squared error (RMSE), peak signal-to-noise ratio (PSNR) in decibels

(dB), and structural similarity (SSIM). MSE, MAE, and RMSE results also have 95% bootstrap confidence intervals, given by the two values in which the range of taken intervals most appears, shown to the right of the average value given in the table. To calculate the average metric for each of the metrics, the metrics for each of the test cases are added together and divided by the number of test cases in total to get an overall mean value for each of the measurement methods. The results for the test cases averaged together are seen in Table 4.2 in each of the respective network versions based on the split of data used.

Table 4.2: Lung Thickness Test Metrics on Synthetic CXRs

Algorithm	***U-Net RNN (95/5 Split)***	***U-Net RNN (90/10 Split)***	***U-Net RNN (80/20 Split)***
MSE	0.0047 [0.0020 - 0.0125]	0.0133 [0.0101 - 0.0192]	0.0520 [0.0481-0.0586]
MAE	0.0301 [0.0242-0.419]	0.0613 [0.0548 - 0.0720]	0.1297 [0.1228 - 0.1398]
RMSE	0.0446 [0.0377-0.0634]	0.0837 [0.0779 - 0.0994]	0.1765 [0.1682 - 0.1909]
PSNR [dB]	26.6652	20.7344	14.0539
SSIM	0.8529	0.7790	0.5582

The predictions and the actual lung thickness values are then evaluated visually. To do this, an example from the 95/5 split network is selected for qualitative comparisons. This example is seen from the 31st test case correlating to LIDC-IDRI case 0346, which gives a very accurate prediction of relative 2D lung thickness within the 95/5 split network. This is visually evaluated through the comparison of lung depth isocontours, which shows 10 total, as well as the lung thickness data in 3D space. These 3D visuals are compared from the sagittal-coronal plane as well as the coronal/frontal plane to give an accurate. The comparison between isocontours can be seen in Figure 4.1, whereas the 3D visuals are seen in Figures 4.2 and 4.3.

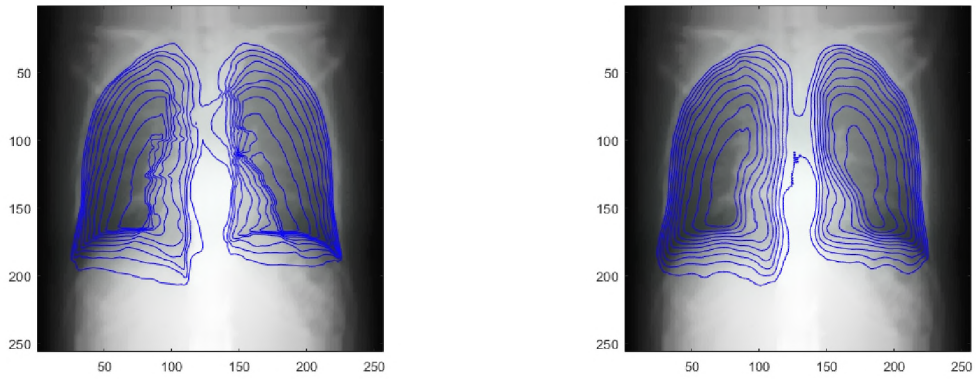

(a) (b)

Figure 4.1: Utilizing 10 sets of isocontours, the DRR is overlayed with the relative lung depths for the (a) actual lung thickness and the (b) predicted lung thickness. The isocontours give a rounded view of the lungs projecting 3D values into 2D space.

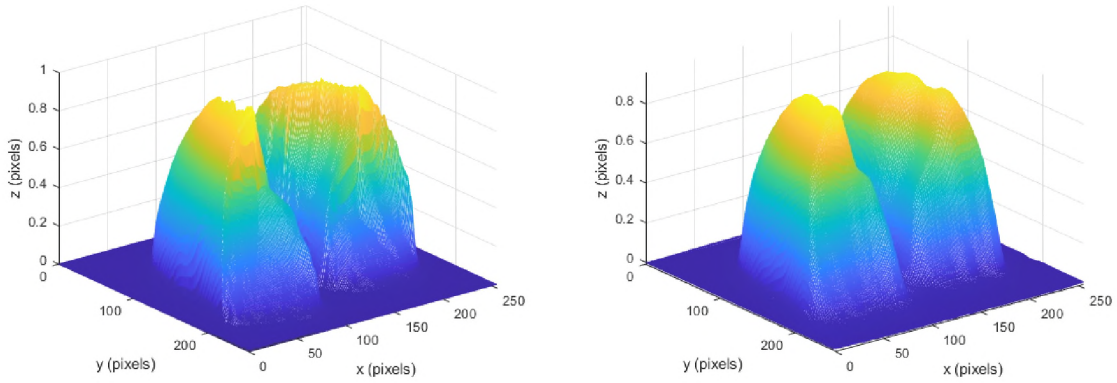

(a) (b)

Figure 4.2: Showing the relative 2D lung thickness values in a 3D space, the (a) actual lung thickness values and the (b) predicted lung thickness values are displayed from the Sagittal-Coronal plane view. Of particular note is the smoother texture of the lung thickness in the predicted lung depth compared to the actual lung depth; the U-Net RNN predictions do not give the grainy, imperfect texture of the lungs that the actual values do.

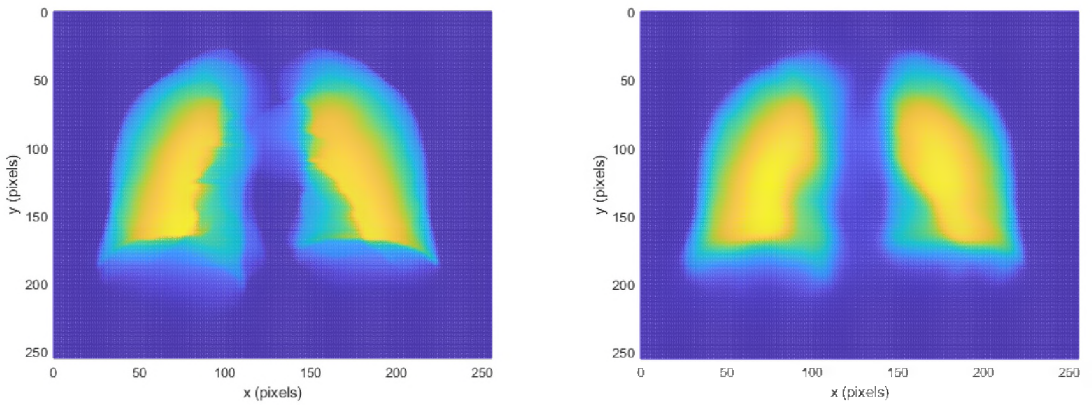

Figure 4.3: The relative 2D lung thickness values are displayed using a heat map to visualize each pixel in which the lung is present as well as the relative height of that pixel. The (a) actual lung thickness values show more layering of the lung itself with clear hazings between viewable areas of the lungs while the (b) predicted lung thickness values give a much more sanitized look to the lungs almost like segmented lung masks.

Figure 4.1 shows the lung depths with 10 isocontours against the synthetic CXR. The left shows the actual lung depth whereas the right shows the predicted. The predicted set of isocontours appears to be much more rounded with much fewer jagged and straight lines. The actual set is biological so they are more erratic across the lungs, with some almost crisscrossing and overlapping.

Figures 4.2 and 4.3 show the same test case with the 2D lung thickness displayed in 3D space, with Figure 4.2 from the sagittal-coronal plane and Figure 4.3 from the coronal, or frontal, plane. Just as in the isocontours, the actual lungs are displayed on the left with the predicted set on the right. Overall, the predicted and the actual lungs look remarkably similar. From the sagittal-coronal view, the actual lungs prove to have more jagged edges that move around the surfaces of the lungs. The predicted lungs are much smoother, with

what appears to be slightly thicker lungs, which may allow for smoother surfaces compared to the jagged set in the actual lungs. As for the frontal view, the actual lung depth shows a very crisp image with many parts of the lung seemingly layered over one another. In contrast, the predicted lungs appear to be completely melded together with faded sections from the peaks to the bottom of the lungs.

CHAPTER V

CONCLUSIONS AND FUTURE WORK

In this thesis, an efficient way of estimating relative 2D lung thickness from CXRs made via DRRs using a U-Net RNN is presented. By utilizing the LIDC CT scans, CT scan data is placed into a CT two synthetic CXR conversion process to properly acquire several DRRs. The same CT data is also processed using CAD algorithms from FlyerScan to calculate a 3D segmentation of the lungs. This data is placed into the same CT to synthetic CXR conversion, via the derived Beer Lambert's law in order to get relative 2D lung thickness values. Both of these are separated into training and testing groups to be placed into a 5-layer U-Net RNN that allows for image to image-regression to take place after proper training. The performance of the test cases, given by the low MSE, MSA, and RMSE values in 4.2, show that the network does an efficient and accurate job of recreating the relative 2D lung thicknesses using just the synthetic CXR data inputted. This is further secured when comparing the test results between the actual 2D lung thickness array values and those that are predicted by the network qualitatively in Figures 4.1, 4.2, and 4.3.

This network potentially serves as a new method in which CAD algorithms can move forward. By integrating this deep learning model with CAD algorithms for nodule detection, the ability for potential nodule locations to be referenced on a relative 2D lung thickness map allows for an additional characteristic to aid in classifying between possible positive and negative nodule detections in lungs, with thicker regions providing potentially higher likelihoods of nodule growth and thinner regions providing potentially lower likelihoods. This would allow for more data to be derived from 2D CXR images when 3D-compiled CT scan data is not available for a patient. Furthermore, this can ensure patients get less of a

radiation dose from more X-ray scans, via CXRs or CT scans, when the same information can be found from a single X-ray instead.

In terms of future work, integrating this algorithm into CAD algorithms could prove to be beneficial in increasing the performance of nodule detection algorithms. Another idea is finding a way to ensure accurate millimeter-levels of data for the lung thickness values rather than using relative values, which could assist lung morphology predictions further using just X-ray data. Another method of increasing the performance of the U-Net RNN model would be partnering with hospitals or creating new public databases that have matching CT scan data with accompanying X-ray data. This would allow for more training and testing data to be placed into the model, possibly increasing performance. Furthermore, the addition of real CXRs that match CT scan data, especially when taken in close succession and similar conditions, would ensure that a model could be created that was based on real-world data rather than a hybrid mix of real-world values derived into synthetic outputs.

BIBLIOGRAPHY

[1] S. Hu, E. Hoffman, and J. Reinhardt, "Automatic lung segmentation for accurate quantitation of volumetric x-ray ct images," *IEEE Transactions on Medical Imaging*, vol. 20, no. 6, pp. 490–498, June 2001.

[2] B. N. Narayanan, R. C. Hardie, V. Krishnaraja, C. Karam, and V. S. P. Davuluru, "Transfer-to-transfer learning approach for computer aided detection of covid-19 in chest radiographs," *AI*, vol. 1, no. 4, pp. 539–557, 2020. [Online]. Available: https://www.mdpi.com/2673-2688/1/4/32

[3] R. J. Pierce, D. J. Brown, M. Holmes, G. Cumming, and D. M. Denison, "Estimation of lung volumes from chest radiographs using shape information," *Thorax*, vol. 34, no. 6, pp. 726–734, Dec. 1979.

[4] M. S. De Silva, B. N. Narayanan, and R. C. Hardie, "A patient-specific algorithm for lung segmentation in chest radiographs," *AI*, vol. 3, no. 4, pp. 931–947, 2022. [Online]. Available: https://www.mdpi.com/2673-2688/3/4/55

[5] R. C. Hardie, A. T. Trout, J. R. Dillman, B. N. Narayanan, and A. A. Tanimoto, "Performance analysis in children of traditional and deep learning ct lung nodule computer-aided detection systems trained on adults," *American Journal of Roentgenology*, vol. 222, no. 2, p. e2330345, 2024, pMID: 37991333. [Online]. Available: https://doi.org/10.2214/AJR.23.30345

[6] B. Segal, D. M. Rubin, G. Rubin, and A. Pantanowitz, "Evaluating the clinical realism of synthetic chest X-Rays generated using progressively growing GANs," *SN Comput Sci*, vol. 2, no. 4, p. 321, jun 2021.

[7] Y. Karbhari, A. Basu, Z. W. Geem, G.-T. Han, and R. Sarkar, "Generation of synthetic chest x-ray images and detection of covid-19: A deep learning based approach," *Diagnostics*, vol. 11, no. 5, 2021. [Online]. Available: https://www.mdpi.com/2075-4418/11/5/895

[8] J. M. Galvin, C. Sims, G. Dominiak, and J. S. Cooper, "The use of digitally reconstructed radiographs for three-dimensional treatment planning and ct-simulation," *International Journal of Radiation Oncology*Biology*Physics*, vol. 31, no. 4, pp. 935–942, 1995. [Online]. Available: https://www.sciencedirect.com/science/article/pii/0360301694005036

[9] X. Li, L.-h. Zhou, X. Zhen, and W.-t. Lu, "The generation of digitally reconstructed radiographs with six parameters," in *2010 4th International Conference on Bioinformatics and Biomedical Engineering*, June 2010, pp. 1–4.

[10] D. Staub and M. J. Murphy, "A digitally reconstructed radiograph algorithm calculated from first principles," *Med Phys*, vol. 40, no. 1, p. 011902, Jan. 2013.

[11] M. I. Campo, J. Pascau, and R. S. J. Estépar, "Emphysema quantification on simulated x-rays through deep learning techniques," in *2018 IEEE 15th International Symposium on Biomedical Imaging (ISBI 2018)*, April 2018, pp. 273–276.

[12] O. Gozes and H. Greenspan, "Lung structures enhancement in chest radiographs via ct based fcnn training," in *Image Analysis for Moving Organ, Breast, and Thoracic Images*, D. Stoyanov, Z. Taylor, B. Kainz, G. Maicas, R. R. Beichel, A. Martel, L. Maier-Hein, K. Bhatia, T. Vercauteren, O. Oktay, G. Carneiro, A. P. Bradley, J. Nascimento, H. Min, M. S. Brown, C. Jacobs, B. Lassen-Schmidt, K. Mori, J. Petersen, R. San José Estépar, A. Schmidt-Richberg, and C. Veiga, Eds. Cham: Springer International Publishing, 2018, pp. 147–158.

[13] ——, "Bone structures extraction and enhancement in chest radiographs via cnn trained on synthetic data," in *2020 IEEE 17th International Symposium on Biomedical Imaging (ISBI)*, 2020, pp. 858–861.

[14] O. Dorgham, M. Ryalat, and M. A. Naser, "Automatic body segmentation for accelerated rendering of digitally reconstructed radiograph images," *Informatics in Medicine Unlocked*, vol. 20, p. 100375, 2020. [Online]. Available: https://www.sciencedirect.com/science/article/pii/S2352914820302446

[15] L. Levine and M. Levine, "DRRGenerator: A three-dimensional slicer extension for the rapid and easy development of digitally reconstructed radiographs," *J Clin Imaging Sci*, vol. 10, p. 69, Oct. 2020.

[16] E. Sogancioglu, K. Murphy, E. Th Scholten, L. H. Boulogne, M. Prokop, and B. van Ginneken, "Automated estimation of total lung volume using chest radiographs and deep learning," *Med Phys*, vol. 49, no. 7, pp. 4466–4477, Apr. 2022.

[17] O. Ronneberger, P. Fischer, and T. Brox, "U-net: Convolutional networks for biomedical image segmentation," in *Medical Image Computing and Computer-Assisted Intervention – MICCAI 2015*, N. Navab, J. Hornegger, W. M. Wells, and A. F. Frangi, Eds. Cham: Springer International Publishing, 2015, pp. 234–241.

[18] B. N. Narayanan and R. C. Hardie, "A computationally efficient u-net architecture for lung segmentation in chest radiographs," in *2019 IEEE National Aerospace and Electronics Conference (NAECON)*, July 2019, pp. 279–284.

[19] M. H. Asnawi, A. A. Pravitasari, G. Darmawan, T. Hendrawati, I. N. Yulita, J. Suprijadi, and F. A. L. Nugraha, "Lung and infection CT-Scan-Based segmentation with 3D UNet architecture and its modification," *Healthcare (Basel)*, vol. 11, no. 2, Jan. 2023.

[20] W. Yao, Z. Zeng, C. Lian, and H. Tang, "Pixel-wise regression using u-net and its application on pansharpening," *Neurocomputing*, vol. 312, pp. 364–371, 2018. [Online]. Available: https://www.sciencedirect.com/science/article/pii/S0925231218307008

[21] S. Ghimire and S. Subedi, "Estimating lung volume capacity from x-ray images using deep learning," *Quantum Beam Science*, vol. 8, no. 2, 2024. [Online]. Available: https://www.mdpi.com/2412-382X/8/2/11

[22] T. Messay, R. C. Hardie, and T. R. Tuinstra, "Segmentation of pulmonary nodules in computed tomography using a regression neural network approach and its application to the lung image database consortium and image database resource initiative dataset," *Medical Image Analysis*, vol. 22, no. 1, pp. 48–62, 2015. [Online]. Available: https://www.sciencedirect.com/science/article/pii/S1361841515000316

[23] R. C. Hardie, S. K. Rogers, T. Wilson, and A. Rogers, "Performance analysis of a new computer aided detection system for identifying lung nodules on chest radiographs," *Medical Image Analysis*, vol. 12, no. 3, pp. 240–258, 2008. [Online]. Available: https://www.sciencedirect.com/science/article/pii/S136184150700103X

[24] B. N. Narayanan, R. C. Hardie, T. M. Kebede, and M. J. Sprague, "Optimized feature selection-based clustering approach for computer-aided detection of lung nodules in different modalities," *Pattern Analysis and Applications*, vol. 22, pp. 559–571, 2019.

[25] T. Okumura, T. Miwa, J.-I. Kako, S. Yamamoto, R. Matsumoto, Y. Tateno, T. Iinuma, and T. Matsumoto, "Automatic detection of lung cancers in chest ct images by variable n-quoit filter," in *Proceedings. Fourteenth International Conference on Pattern Recognition (Cat. No. 98EX170)*, vol. 2. IEEE, 1998, pp. 1671–1673.

[26] B. N. Narayanan, R. C. Hardie, and T. M. Kebede, "Analysis of various classification techniques for computer aided detection system of pulmonary nodules in ct," in *2016 IEEE National Aerospace and Electronics Conference (NAECON) and Ohio Innovation Summit (OIS)*. IEEE, 2016, pp. 88–93.

[27] B. Narayanan, V. Davuluru, and R. Hardie, "Two-stage deep learning architecture for pneumonia detection and its diagnosis in chest radiographs. med imaging 2020: Imaging inf healthcare, research, appl 11318: 113180g," *International Society for Optics and Photonics*, 2020.

[28] L. L. G. Oliveira, S. A. e Silva, L. H. V. Ribeiro, R. M. de Oliveira, C. J. Coelho, and A. L. S. Andrade, "Computer-aided diagnosis in chest radiography for detection of childhood pneumonia," *International journal of medical informatics*, vol. 77, no. 8, pp. 555–564, 2008.

[29] B. Van Ginneken, B. T. H. Romeny, and M. A. Viergever, "Computer-aided diagnosis in chest radiography: a survey," *IEEE Transactions on medical imaging*, vol. 20, no. 12, pp. 1228–1241, 2001.

[30] M. Giger and H. MacMahon, "Image processing and computer-aided diagnosis," *Radiologic Clinics of North America*, vol. 34, no. 3, pp. 565–596, 1996.

[31] L. Monnier-Cholley, H. MacMahon, S. Katsuragawa, J. Morishita, T. Ishida, and K. Doi, "Computer-aided diagnosis for detection of interstitial opacities on chest radiographs." *AJR. American journal of roentgenology*, vol. 171, no. 6, pp. 1651–1656, 1998.

[32] P. Rajpurkar, J. Irvin, K. Zhu, B. Yang, H. Mehta, T. Duan, D. Ding, A. Bagul, C. Langlotz, K. Shpanskaya *et al.*, "Chexnet: Radiologist-level pneumonia detection on chest x-rays with deep learning," *arXiv preprint arXiv:1711.05225*, 2017.

[33] B. N. Narayanan, M. S. De Silva, R. C. Hardie, N. K. Kueterman, and R. Ali, "Understanding deep neural network predictions for medical imaging applications," *arXiv preprint arXiv:1912.09621*, 2019.

[34] Q. Guan, Y. Huang, Z. Zhong, Z. Zheng, L. Zheng, and Y. Yang, "Diagnose like a radiologist: Attention guided convolutional neural network for thorax disease classification," *arXiv preprint arXiv:1801.09927*, 2018.

[35] M. Javaid, M. Javid, M. Z. U. Rehman, and S. I. A. Shah, "A novel approach to cad system for the detection of lung nodules in ct images," *Computer methods and programs in biomedicine*, vol. 135, pp. 125–139, 2016.

[36] B. Van Ginneken, S. G. Armato III, B. de Hoop, S. van Amelsvoort-van de Vorst, T. Duindam, M. Niemeijer, K. Murphy, A. Schilham, A. Retico, M. E. Fantacci *et al.*, "Comparing and combining algorithms for computer-aided detection of pulmonary nodules in computed tomography scans: the anode09 study," *Medical image analysis*, vol. 14, no. 6, pp. 707–722, 2010.

[37] S. G. Armato, M. L. Giger, C. J. Moran, J. T. Blackburn, K. Doi, and H. MacMahon, "Computerized detection of pulmonary nodules on ct scans," *Radiographics*, vol. 19, no. 5, pp. 1303–1311, 1999.

[38] S. G. Armato III, G. McLennan, L. Bidaut, M. F. McNitt-Gray, C. R. Meyer, A. P. Reeves, B. Zhao, D. R. Aberle, C. I. Henschke, E. A. Hoffman, E. A. Kazerooni, H. MacMahon, E. J. R. van Beek, D. Yankelevitz, A. M. Biancardi, P. H. Bland, M. S. Brown, R. M. Engelmann, G. E. Laderach, D. Max, R. C. Pais, D. P.-Y. Qing, R. Y. Roberts, A. R. Smith, A. Starkey, P. Batra, P. Caligiuri, A. Farooqi, G. W. Gladish, C. M. Jude, R. F. Munden, I. Petkovska, L. E. Quint, L. H. Schwartz, B. Sundaram, L. E. Dodd, C. Fenimore, D. Gur, N. Petrick, J. Freymann, J. Kirby, B. Hughes, A. Vande Casteele, S. Gupte, M. Sallam, M. D. Heath, M. H. Kuhn, E. Dharaiya, R. Burns, D. S. Fryd, M. Salganicoff, V. Anand, U. Shreter, S. Vastagh, B. Y. Croft, and L. P. Clarke, "The lung image database consortium (lidc) and image database resource initiative (idri): A completed reference database of lung nodules on ct scans," *Medical Physics*, vol. 38, no. 2, pp. 915–931, 2011. [Online]. Available: https://aapm.onlinelibrary.wiley.com/doi/abs/10.1118/1.3528204

[39] R. Wiemker, P. Rogalla, R. Opfer, A. Ekin, V. Romano, and T. Bülow, "Comparative performance analysis for computer-aided lung nodule detection and segmentation on ultra-low-dose vs. standard dose ct," in *Medical Imaging 2006: Image Perception, Observer Performance, and Technology Assessment*, vol. 6146. SPIE, 2006, pp. 27–36.

[40] M. Das, G. Mühlenbruch, A. H. Mahnken, T. G. Flohr, L. Gündel, S. Stanzel, T. Kraus, R. W. Günther, and J. E. Wildberger, "Small pulmonary nodules: effect of two computer-aided detection systems on radiologist performance," *Radiology*, vol. 241, no. 2, pp. 564–571, 2006.

[41] R. Yuan, P. M. Vos, and P. L. Cooperberg, "Computer-aided detection in screening ct for pulmonary nodules," *American Journal of Roentgenology*, vol. 186, no. 5, pp. 1280–1287, 2006.

[42] J. Gurung, A. Maataoui, M. Khan, A. Wetter, M. Harth, V. Jacobi, and T. Vogl, "Automated detection of lung nodules in multidetector ct: influence of different reconstruction protocols on performance of a software prototype," in *RöFo-Fortschritte auf dem Gebiet der Röntgenstrahlen und der bildgebenden Verfahren*, vol. 178, no. 01. © Georg Thieme Verlag KG Stuttgart · New York, 2006, pp. 71–77.

[43] R. Opfer and R. Wiemker, "Performance analysis for computer-aided lung nodule detection on lidc data," in *Medical Imaging 2007: Image Perception, Observer Performance, and Technology Assessment*, vol. 6515. SPIE, 2007, pp. 396–404.

[44] B. Sahiner, H.-P. Chan, L. M. Hadjiiski, P. N. Cascade, E. A. Kazerooni, A. R. Chughtai, C. Poopat, T. Song, L. Frank, J. Stojanovska *et al.*, "Effect of cad on radiologists' detection of lung nodules on thoracic ct scans: analysis of an observer performance study by nodule size," *Academic radiology*, vol. 16, no. 12, pp. 1518–1530, 2009.

[45] S. Buhmann, P. Herzog, J. Liang, M. Wolf, M. Salganicoff, C. Kirchhoff, M. Reiser, and C. H. Becker, "Clinical evaluation of a computer-aided diagnosis (cad) prototype for the detection of pulmonary embolism," *Academic radiology*, vol. 14, no. 6, pp. 651–658, 2007.

[46] A. M. Schilham, B. Van Ginneken, and M. Loog, "A computer-aided diagnosis system for detection of lung nodules in chest radiographs with an evaluation on a public database," *Medical Image Analysis*, vol. 10, no. 2, pp. 247–258, 2006.

[47] B. N. Narayanan, M. S. De Silva, R. C. Hardie, and R. Ali, "Ensemble method of lung segmentation in chest radiographs," in *NAECON 2021 - IEEE National Aerospace and Electronics Conference*, 2021, pp. 382–385.

[48] M. S. De Silva, B. N. Narayanan, and R. C. Hardie, "A patient-specific algorithm for lung segmentation in chest radiographs," *AI*, vol. 3, no. 4, pp. 931–947, 2022. [Online]. Available: https://www.mdpi.com/2673-2688/3/4/55

[49] R. C. Hardie, A. T. Trout, J. R. Dillman, B. N. Narayanan, and A. A. Tanimoto, "Performance analysis in children of traditional and deep learning ct lung nodule computer-aided detection systems trained on adults," *American Journal of Roentgenology*, vol. 222, no. 2, p. e2330345, 2024, pMID: 37991333. [Online]. Available: https://doi.org/10.2214/AJR.23.30345

[50] T. Messay, R. C. Hardie, and S. K. Rogers, "A new computationally efficient cad system for pulmonary nodule detection in ct imagery," *Medical Image Analysis*, vol. 14, no. 3, pp. 390–406, 2010. [Online]. Available: https://www.sciencedirect.com/science/article/pii/S1361841510000198

[51] M. Schultheiss, P. Schmette, T. Sellerer, R. Schick, K. Taphorn, K. Mechlem, L. Birnbacher, B. Renger, M. R. Makowski, F. Pfeiffer, and D. Pfeiffer, "Per-pixel lung thickness and lung capacity estimation on chest x-rays using convolutional neural networks," 2022.

[52] M. I. Campo, J. Pascau, and R. S. J. Estépar, "Emphysema quantification on simulated x-rays through deep learning techniques," in *2018 IEEE 15th International Symposium on Biomedical Imaging (ISBI 2018)*, 2018, pp. 273–276.